ACS OMEGA

Open Access

http://pubs.acs.org/journal/acsodf

Article

Tumor-Targeted Magnetic Micelles for Magnetic Resonance Imaging, Drug Delivery, and Overcoming Multidrug Resistance

Hui-Qin Liu,[▽] Xi-Dong Wu,[▽] Xue-Wen Fang,[▽] Yun-Song An, Meng Xia, Xiao-Hua Luo, Jun-Zheng Li,* Guan-Hai Wang,* and Tao Liu*

Cite This: *ACS Omega* 2024, 9, 49566−49579

Read Online

ACCESS | Metrics & More | Article Recommendations | Supporting Information

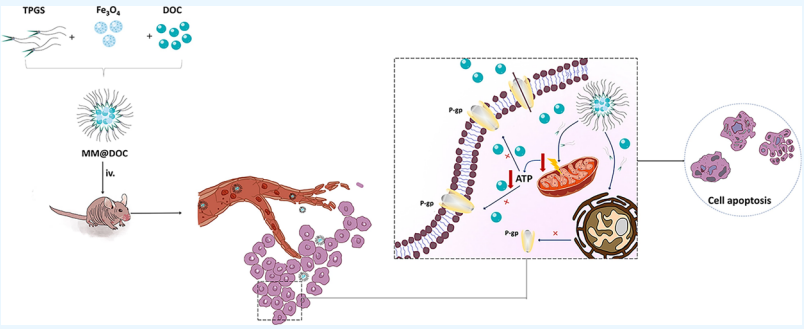

ABSTRACT: Nasopharyngeal carcinoma (NPC) is prevalent in Southern China. Unfortunately, current treatments encounter multidrug resistance (MDR). Overexpression of P-glycoprotein (P-gp), resulting in the efflux of chemotherapy drugs, is one of the significant mechanisms causing MDR. D-α-Tocopheryl poly(ethylene glycol) 1000 succinate (TPGS) has been demonstrated to effectively inhibit P-gp expression. The objectives of this study are to improve tumor MRI imaging, optimize docetaxel (DOC) administration, and target P-gp to overcome NPC resistance. Multifunctional micelles of TPGS (MM@DOC), loaded with magnetic nanoparticles, were synthesized for the targeted delivery of the first-line anticancer drug. MM@DOC exhibited greater toxicity and induced higher levels of apoptosis in DOC-resistant NPC cells (C666−1/DOC) compared to DOC. MM@DOC loaded with magnetic nanoparticles improved the quality of tumor MRI imaging. MM@DOC also demonstrated significant antitumor effects in nude mice with C666−1/DOC NPC. In conclusion, MM@DOC exhibited promising inhibitory effects on resistant tumors both in vitro and in vivo, optimized tumor MRI imaging, and showed great potential in drug delivery and overcoming resistance.

1. INTRODUCTION

The incidence pattern of nasopharyngeal carcinoma (NPC) shows a notable geographical distribution, with the most affected region being Southern China, where the annual incidence is approximately 3.0 cases per 100,000 individuals.[1,2] The comprehensive approach of radiotherapy combined with chemotherapy is the main clinical treatment strategy for NPC nowadays. However, due to multidrug resistance and the metastatic nature of NPC, the five-year average survival rate of middle and advanced NPC patients remains low ranging from 20 to 30%.[3] The rate of distant metastasis remains above 20% even after treatment.[4,5]

Docetaxel (DOC) is a widely used first-line chemotherapeutic drug[6] employed in NPC treatment.[7−9] DOC binds to the beta-tubulin subunit of tubulin polymers. In contrast to vinca alkaloids, which prevent microtubule assembly, DOC shortens the lag time and shifts the dynamic equilibrium between tubulin dimers and microtubules toward polymerization, thus stabilizing microtubules.[10] It inhibits cell proliferation at the metaphase/anaphase boundary and then results in apoptosis or programmed cell death.[11] However, the use of taxanes in chemotherapy is limited due to their relatively low absorption, systemic side effects resulting from lack of targeting, and tumor drug resistance.[12,13] Despite DOC's significant contribution to cancer treatment, delivering chemotherapeutic agents to specific sites for targeted treatment, minimizing toxic effects, and overcoming drug resistance remain active areas of research.

Multiple drug resistance (MDR) presents a significant clinical difficulty in cancer chemotherapy, resulting in lower sensitivity to chemotherapy and higher side effects. Statistical data indicate that more than 90% of deaths in chemotherapy patients are attributed to drug resistance. Resistance mechanisms primarily involve increased drug efflux, genetic

Received: August 14, 2024
Revised: November 16, 2024
Accepted: November 25, 2024
Published: December 9, 2024

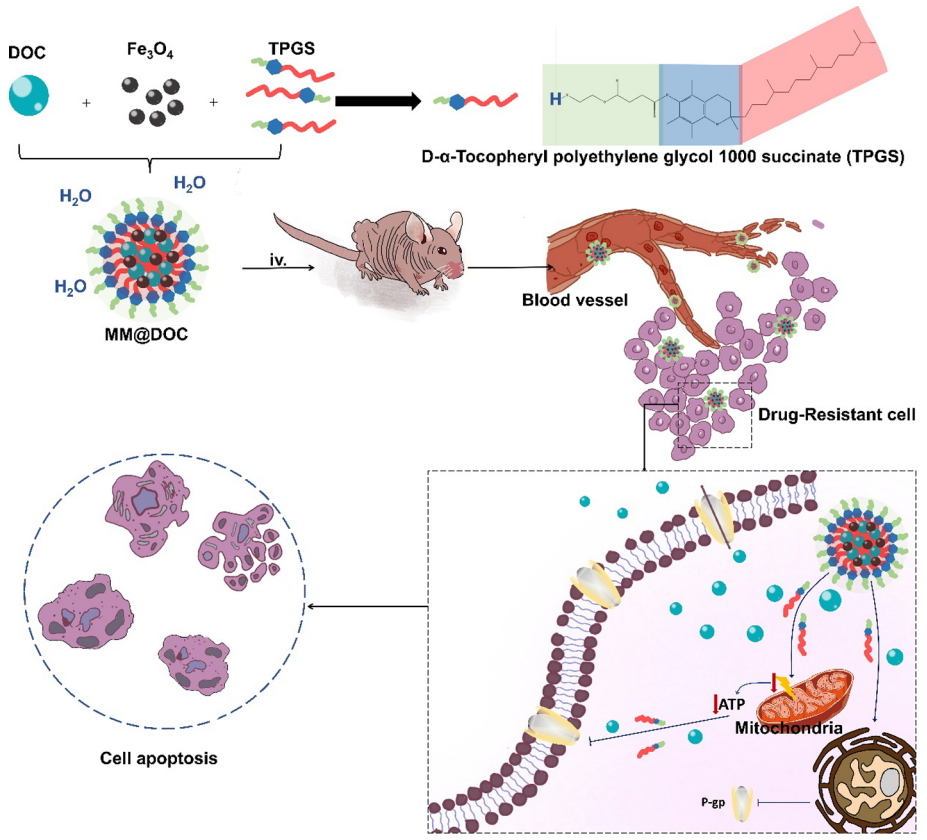

Figure 1. Construction, in vivo release, and mechanism of MM@DOC.

factors, and growth factors.[3,14,15] Studies have found that DOC resistance is primarily associated with ATP-binding cassette transporters (ABC transporters).[16−19] ABC transporters comprise two components: cytoplasmic nucleotide-binding domains (NBDs), which bind and hydrolyze ATP, and transmembrane domains (TMDs), which recognize and transport substrates. The quantity of ABC transporters indicates drug uptake and release.[20] P-glycoprotein (P-gp) is among the most extensively studied ABC transporters. Overexpression of P-gp can result in increased drug efflux. Thus, inhibiting P-gp expression or function may reverse drug resistance.[21,22]

D-α-Tocopheryl polyethylene glycol 1000 succinate (TPGS) is primarily utilized in cancer therapy for inhibiting P-gp.[9] The P-gp inhibiting ability of TPGS enhances drug accumulation and treatment efficacy across different cancer types.[23,24] Additionally, TPGS possesses a lipophilic alkyl tail and a hydrophilic polar head, enabling it to encapsulate hydrophobic drugs into spherical micelles with a core−shell structure in aqueous solutions.[25−27] It has been shown to positively affect the solubilization of DOC.[9,23] Moreover, TPGS can enhance the release of ROS-responsive drugs in tumor cells, thereby enhancing the efficacy of PTX in inhibiting head and neck tumors.[26] Furthermore, TPGS has proven its important role in chemotherapy by inducing the arrest of the cell cycle and promoting apoptosis.[24] Undoubtedly, TPGS stands as a potent candidate for anticancer drug delivery systems. Magnetic nanoparticles (MNPs), as a type of magnetic substance, can increase the magnetic field, thereby improving MRI contrast, sensitivity, and resolution.[28] The small diameters of MNPs have been widely utilized as a negative contrast agent. In addition, MNPs have excellent biological safety and surface modifiability, which shows great application value in biomedicine.[29−31]

This study proposes a new medication delivery system aimed at increasing treatment efficacy, reducing DOC toxicity, enhancing the biocompatibility of DOC, and improving drug delivery. Figure 1 illustrates a novel drug delivery system in which DOC and MNPs are loaded into TPGS-formed micelles (MM@DOC). The magnetic characteristics, thermal stability, and crystal structure of the colloid were ascertained, and the structure of MNPs was examined using transmission electron microscopy (TEM). Dynamic light scattering (DLS) was used to measure the MM@DOC particle size, particle size distribution, and zeta (ζ) potential. DOC-resistant cells (C666−1/DOC cells) were cultivated for both in vitro and in vivo investigations in this study. In vitro experiments assessed cytotoxicity and apoptosis, which were tested by MTT assay and flow cytometry. Western blot assay was used to confirm P-gp expression in C666−1/DOC cells. MRI and in vivo fluorescence imaging were utilized to assess the medication distribution in mice. Additionally, the in vivo experiment investigated MDR reversal and biocompatibility. Through the aforementioned experiments, we aimed to explore the value of TPGS in drug delivery and overcome drug resistance. It is proven that the synthesized MM@DOC in this study is useful for MRI imaging and reversal of drug resistance, which brings new ideas for the treatment of NPC drug resistance.

2. MATERIALS AND METHODS

2.1. Materials. DOC was purchased from Aladdin Chemistry Co., Ltd. (Shanghai, China) and used without further purification. TPGS was purchased from Sigma (USA).

https://doi.org/10.1021/acsomega.4c07132
ACS Omega 2024, 9, 49566−49579

0.25% Trypsin-ethylenediamine tetra-acetic acid (Trypsin-EDTA) and 3-[4,5-dimethyl-2-thiazolyl]-2,5-diphenyltetrazolium bromide (MTT) were purchased from Dongguan Kemao Biological Technology Co., Ltd. 100 U/mL penicillin G sodium, fetal bovine serum (FBS), Dulbecco's modified Eagle's medium (DMEM), Annexin V FITC-A, propidium iodide (PI), and Dulbecco's phosphate-buffered saline (PBS) were purchased from Guangzhou Ward Biological Technology Co., Ltd.

DOC-resistant NPC cell line C666−1 cells were purchased from the Shanghai Institute of Biochemistry and Cell Biology (Shanghai, China) and provided the technology for constructing drug-resistant cell lines. Those cells were saved by the Key Biologic Laboratory of Blood Tumor Cell of Jiangxi Province, Nanchang 330006, China. Female-specific pathogen-free BALB/c mice were provided by Hunan Shrek Jingda Experimental Animal Co, Ltd. (Hunan, China; license number: SCXK (Xiang) 2019-0004) and fed in the Experimental Animal Center of Jiangxi Testing Center of Medical Instruments (Jiangxi Institute of Materia Medica; license number: SCXK (Gan) 2016-0002).

2.2. Preparation of MM@DOC. MNPs were prepared following a previous study, and a modified method was employed to synthesize Fe_3O_4.[29,32] $Fe(acac)_3$ was chosen to be the organometallic precursor material, 1,2-hexadecanediol was used as the surfactant, and oleic acid as well as oleylamine were selected to be the disperser. Through thermal decomposition, the aforementioned components were added to phenyl ether and stirred under a nitrogen stream to yield a black precipitate. The dark precipitate was subsequently centrifuged and purified using ethanol as a solvent. The centrifugation and dissolution stages were repeated after the purified black precipitate was dissolved in hexane. Initially, hydrophobic Fe_3O_4 nanoparticles with a diameter of 6 nm were synthesized. To synthesize 8 nm Fe_3O_4 nanoparticles, the above solution was added to a solution of 6 nm Fe_3O_4 nanoparticles dispersed in hexane, and the previous steps were repeated. Finally, 8 nm Fe_3O_4 nanoparticles were obtained via 6 nm Fe_3O_4 seeds and prepared for the following synthesis experiments.

To prepare MM@DOC, 90 mg of TPGS was dissolved in 5 mL of pure water to form a micellar aqueous solution. Due to their hydrophobic nature, 5 mg of 8 nm Fe_3O_4 and 5 mg of DOC were dissolved in 5 mL of 100% DMSO. Subsequently, the mixture was stirred thoroughly until fully dissolved. The mixture of Fe_3O_4 and DOC was gradually dropped into the micellar aqueous solution. The samples were then shaken at 150 rpm for 12 h to encapsulate MNPs and DOC within the TPGS micelles. Purification and drying were carried out by rotary distillation and an empty chamber to remove the excess solvent. Dialysis was used to further purify it following a series of initial purifications and the elimination of DMSO. Finally, an appropriate mass ratio (8 nm Fe_3O_4: TPGS: DOC = 1:18:1) of MM@DOC was synthesized. The prepared mixture was stored at 4 °C in the refrigerator. Similarly, to prepare MM@DOC carried out with fluorescent agents, an equal quantity of ICG was added during the DOC addition process described above. A similar procedure was used to prepare TPGS-Fe_3O_4 at the proper mass ratio (Fe_3O_4: TPGS = 1:18). They were purified, dried, and preserved in the same way as MM@DOC.

2.3. Evaluation of Encapsulation Efficiency. DOC encapsulation efficiency was performed by the dialysis method and analyzing DOC by high-performance liquid chromatography (HPLC). The mobile phase in the HPLC analysis was made up of acetonitrile: water (55:45, v/v), with a temperature of 35 °C and a wavelength of 230 nm. The C18 reverse phase column (LiChrospher, Merck RP-18) was utilized. 1 mL of the newly synthesized MM@DOC was transferred into a dialysis bag (Mw = 3500) and immersed in 150 mL of 0.5% Tween-80 solution for dialysis at 4 °C for 8 h. After dialysis, the solution inside the dialysis bag was completely transferred. Methanol was added to demulsify, and the content of DOC was ascertained by HPLC. 1 mL of MM@DOC was transferred to a measuring bottle. Then, methanol was added, and DOC content was determined by HPLC. The entrapment efficiency of DOC was 78.6%. The encapsulation efficiency of DOC was tested by the following equations:

$$\text{Encapsulationefficiency}(\%) = \left(\text{Weightofdruginmicelles} \Big/ \text{Initialweightofdrug}\right) \times 100\%$$

2.4. Characterization and Physical and Chemical Properties of Multifunctionalized Magnetic Nanocarriers. The morphology of MNPs was observed by TEM (JEOL, Tokyo, Japan) at 80 kV. The thermal stability of the sample was analyzed by TGA (TGA, PerkinElmer Pyris, USA). 3 mL of the MNPs and MM@DOC were loaded into a particle size measurement container, and their particle size and size distribution as well as zeta (ζ) potential were determined by DLS to evaluate the properties of the nanomedicine.

Five mg of Fe_3O_4, TPGS-Fe_3O_4, and MM@DOC samples under N_2 gas (flow rate = 30 cm^3/min) were tested respectively from 25 to 800 °C at a heating rate of 10 °C/min. The weight of the sample was recorded at different temperature nodes. The crystal lattice property of MM@DOC was analyzed by X-ray powder diffraction (XRD, Siemens D5000) scanned from 0 to 90 (2θ) at 30 kV and 20 mA with the monochromatized Cu Kα radiation (MAC Science, MXP18). Two equal portions of MNPs and MM@DOC were taken respectively and labeled as MNPs-1, MNPs-2, MM@DOC-1, and MM@DOC-2. Magnetic properties of the MNPs and MM@DOC were measured with a vibrating-sample magnetometer (VSM) (Lakeshore, model 7300). Before analysis, the samples underwent lyophilization. The magnetization of the samples was measured as a function of the magnetic field (H, Oe) in the range of −10 to 10 kOe at 298 K (25 °C). For the Fourier transform infrared spectroscopy (FTIR) analysis of MNPs and MM@DOC, a small amount of the above sample powder was mixed with potassium bromide powder and then pressed into thin films. Finally, the films were analyzed using an infrared tester.

2.5. Evaluation of In Vitro Drug Release Kinetics. The quantity of DOC released from MM@DOC was measured by HPLC. 2 mL of TPGS-DOC and MM@DOC suspensions was carefully added into dialysis bags (Mw = 3500), respectively. Then, the dialysis bags were placed in a beaker containing 20 mL of 0.5% Tween-80 PBS (pH = 7.4 and 6.8) solution at 37 ± 0.5 °C. The in vitro release test was conducted using a vibrator at 100 r/min. 2 mL samples were periodically collected, and an equivalent volume of fresh release medium was added at each interval. The release rate of DOC was calculated.

2.6. In Vitro Experiments. *2.6.1. Cell Culture and Construction of DOC-Resistant Cells.* DOC-resistant NPC

https://doi.org/10.1021/acsomega.4c07132
ACS Omega 2024, 9, 49566−49579

cells (C666−1/DOC cells) were generated through a process of natural selection by exposing NPC cells to low doses of drugs over an extended period.[33,34] NPC cell line C666−1 cells were cultivated as parent cells. C666−1 cells were cultured in DMEM at 37 °C in a humidified incubator with 5% CO_2. The medium was supplemented with 10% FBS, 100 U/mL penicillin G sodium, and 0.1 mol/mL of streptomycin sulfate. During mixing, cells were enzymatically detached with 0.25% Trypsin-EDTA and subcultured in a new cell culture dish. The medium was replaced daily.

The value of the IC_{50} of C666−1 was determined by the MTT method. The C666−1 cells were seeded on a 96-well plate at a cell density of 1×10^5 cells per well. After 24 h of attachment, the cells were exposed to varying concentrations of DOC (10, 20, 30, 40, 50, 60, 70, and 80 μg/mL) as shown in Figure S1. After drug action for 48 h, the 5 mg/mL MTT solution was added, and the mixture was incubated for another 4 h. Following the removal of the supernatant, 150 μL of DMSO was applied to each hole. The absorbance (A) of each hole was determined by a microplate reader (BioTek, USA) at a wavelength of 490 nm. The IC_{50} value was calculated according to the MTT curve.

For screening of C666−1/DOC cells, C666−1 cells in the logarithmic growth stage were seeded in 6 mm Petri dishes at a cell density of 1×10^6 cells per well. When the cell density reached 70−80%, the cells were treated with DOC. During the initial dosing stage, cells were cultivated with 1/8, 1/4, and 1/2 of the parent cells' IC_{50} (17.99 μg/mL) value, respectively. The cells were passed 48 h later. Additionally, the dosage regimen continued upon reaching 70−80% cell growth. This procedure was repeated to identify stable, resistant strains. If C666−1 cells could grow normally without significant cell death, the concentration of DOC for the culture could be increased. Eventually, the cells were able to grow steadily and pass in a specific drug concentration after several months of growth. Finally, C666−1 cells were chosen as C666−1/DOC cells in this investigation with an IC_{50} value of 43.58 μg/mL.

2.6.2. Cellular Uptake In Vitro. The uptake of MM@DOC by C666−1/DOC cells over a 6-h period was observed using fluorescence microscopy. C666−1/DOC cells were seeded in 12-well plates. MM@DOC was added when C666−1/DOC cells were in logarithmic growth, and fluorescence was observed 1, 3, and 6 h after drug addition. The fluorescence intensity reflects the cellular uptake of the drug concentration.

2.6.3. Cell Viability Assay. The cytotoxic effect was evaluated using the MTT assay. C666−1/DOC cells were seeded at a density of 1×10^5 cells per well in a 96-well plate with 100 μL of DMEM supplemented with 10% FBS. The cells were cultured in a humidified atmosphere of 5% CO_2 at 37 °C and grown for 24 h. Subsequently, the cells were incubated with DOC, TPGS-Fe_3O_4, MM@DOC, and PBS for 24 h. The DOC concentration ranged from 0.1 to 6.4 μg/mL in both the DOC and the MM@DOC groups. The TPGS concentration ranged from 1.8 to 115.2 μg/mL in both the TPGS-Fe_3O_4 and MM@DOC groups. Cells treated with PBS served as the control group. Following the addition of a 5 mg/mL MTT solution, the mixture was left to incubate for an additional 4 h. The C666−1/DOC cells' viability was evaluated with optical absorbance measured on the microplate reader (BioTek, USA) at a wavelength of 490 nm. The mean OD value of the triplicate samples was determined. The cell viability was calculated according to the following formula:

$$\text{Cellviability}(\%) = \left(\text{OD490sample}/\text{OD490control}\right) \times 100\%$$

2.6.4. Cell Necrosis and Apoptosis Assay. The apoptosis of C666−1/DOC cells was analyzed with Annexin-V-FITC and PI (Beyotime Institute of Biotechnology, Shanghai) by flow cytometry (BD Biosciences, USA). C666−1/DOC cells were seeded in 6-well plates at a density of 2×10^5 cells/well and treated with serum-free DMEM containing TPGS-Fe_3O_4, DOC, or MM@DOC at 37 °C for 24 h. The concentrations of TPGS, Fe_3O_4, and DOC in TPGS-Fe_3O_4 and MM@DOC were 1.8 μg/mL, 0.1 μg/mL, and 0.1 μg/mL, respectively. Cells with PBS treatment served as controls. Then, all cells were trypsinized, collected, and washed with ice-cold PBS three times. The cells were resuspended in 200 μL of binding buffer. Thereafter, 5 μL of Annexin V-FITC and 10 μL of PI were added and mixed for 15 min in the dark. Finally, the stained cells were recorded by flow cytometry within 1 h and analyzed by FlowJo 7.6.1 software.

2.6.5. Western Blot. Western blot analysis was performed for the capacity of TPGS in MM@DOC which influences P-gp expression. C666−1/DOC cells (5×10^4) were seeded in 6-well plates and incubated at 37 °C in 5% CO_2 for 24 h to reach 70% confluence. Cells were treated with DMEM containing PBS, 1.8 μg/mL of Fe_3O_4, and different concentrations of TPGS for 24 h. For Western blot analysis, each cell was centrifuged, lysed twice in cold PBS, and then collected. After separating 20 μL of total protein at 120 V for 40 min on 8% PAGE-SDS gels, the protein was transferred to PVDF membranes (Bio-Rad, USA) at 300 mA for 40 min. Following an hour of incubation in phosphate-buffered saline with Tween-20 (PBST, pH 7.2) containing 5% BSA (Merck, Germany), the membranes were again incubated for a whole night in TBST containing 5% BSA and the appropriate antibodies (P-gp 1:1000 and GAPDH 1:1000). After incubation in 5% BSA in TBST with secondary antibodies (1:5000) for 60 min, bands were visualized using the ECL system (Pierce, USA).

2.7. In Vivo Experiments. *2.7.1. Animal Model Construction.* Twenty-three female 5−6-week-old BALB/c mice weighing 18−20 g were selected to minimize individual differences among animals. C666−1/DOC cells at a concentration of 1.5×10^6 cells/mL in the serum-free medium were subcutaneously injected into the back of the right lower limb of each female nude mouse. Each nude mouse was injected with a tumor volume of 0.2 mL, totaling approximately 3×10^5 drug-resistant NPC cells. Once the tumor volume grew to 20 mm^2 (length × width), the samples were prepared for the following experiments.

2.7.2. MRI and In Vivo Fluorescence. T2-weighted imaging was conducted on tumor-bearing mice intravenously injected with 0.2 mL of MM@DOC nanoparticles to demonstrate the contrast-enhancing capability of MM@DOC. Mice were placed in the prone position, and MRI was performed using a 3T MRI scanner (Discovery MR750; GE Healthcare, Little Chalfont, UK) equipped with a specific four-channel coil (10F-04885; Teshen, Shenzhen, China). Mice were anesthetized by intraperitoneal injection of 10% phenobarbital sodium at a dose of 75 mg/kg before the scan. The first scan (t_0) was done before the administration of MM@DOC nanoparticles (0.2 mL) via the tail vein. After the tail vein injection, the magnet was mounted on the tumor point to retain the nanocarriers at

https://doi.org/10.1021/acsomega.4c07132
ACS Omega 2024, 9, 49566−49579

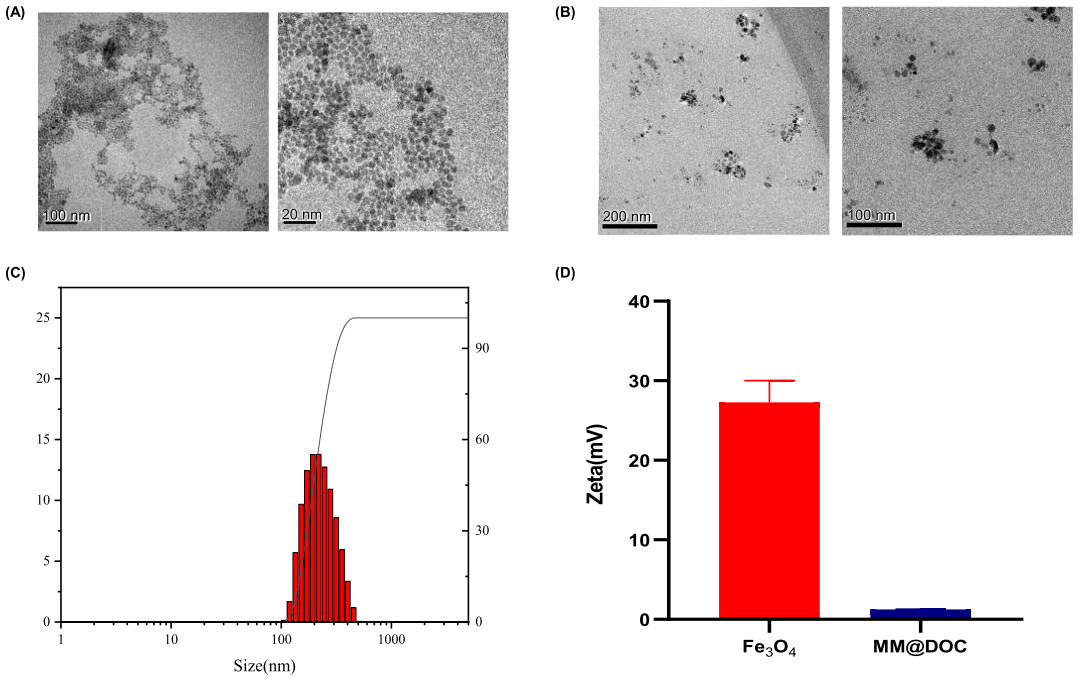

Figure 2. Morphology, particle size, and zeta potential of MM@DOC. (A) TEM photograph of the MNPs (scale bars: 100 and 20 nm). (B) TEM photograph of MM@DOC (scale bars: 200 and 100 nm). (C) Particle size distribution and PDI of MM@DOC. (D) Zeta (ζ) potential of MM@DOC and the MNPs.

the tumor site. The magnet was removed after each scan. The other scans were carried out at 4 h (t_1) and 24 h (t_2) postinjection. Coronal T2-weighted pictures were obtained to examine the imaging of the tumor. After instrument scanning, all tumor-bearing mice were killed with a deep anesthetic painlessly by intraperitoneal injection of 150 mg/kg of 10% phenobarbital sodium.

ICG, the most widely used as a fluorescent tracer, is a nontargeted fluorescent tracer with a vascular pool effect. Although it does not bind to tumor cells directly, it does accumulate in areas with high vascular density and exhibits safety.[35] Using the IVIS Spectrum image system (Maestro, USA) with an emission fluorescence signal collected from 500 to 750 nm and the 455 nm excitation filter, fluorescence imaging was used to determine the body distribution and metabolism of an MM@DOC nanoparticle-based therapeutic system in tumor-bearing mice. The tumor-bearing mice were intravenously injected with ICG-MM@DOC nanoparticles (0.2 mL). Mice in each group were deeply anesthetized with gaseous chloral hydrate. At the scheduled time, 0 (t_0), 1 (t_1), 4 (t_2), 8 (t_3), 12 (t_4), and 24 h (t_5), the mice were anesthetized and placed in the in vivo imaging system to capture the images. Images were analyzed with Living Image Software. After instrument scanning, all tumor-bearing mice were killed with a deep anesthetic painlessly by intraperitoneal injection of 150 mg/kg of phenobarbital.

2.7.3. In Vivo Therapy. C666−1/DOC tumor-bearing nude mice were randomly divided into four groups (n = 5). The mice were given intravenous injections of 100 mg/kg of MM@DOC, PBS, 5 mg/kg of DOC, and 95 mg/kg of TPGS-Fe_3O_4 once the tumor volume had grown to 20 mm^2 (length × breadth). The PBS group served as the control group. All formulations were injected three times a week for a continuous period of 30 days. The body weight and tumor size of tumor-bearing mice were measured every other day. Following the final experiment, tumor-bearing mice were executed by a deep anesthetic painlessly by intraperitoneal injection of 150 mg/kg of phenobarbital. Then, the tumor was aseptically excised, photographed, and weighed. The tumor inhibition rate and tumor volume were calculated. The tumor volume was calculated as

$$\text{Tumorvolume} = (L \times W^2) \times \pi/6$$

L: the longest diameter of the tumors; W: the shortest diameter of the tumors.

2.7.4. Biochemical Assays of Tumor-Bearing Mice. After the last dose was given, blood samples were taken from the orbital venous plexus of tumor-bearing mice for blood biochemical tests in order to confirm the biological safety of the medications. Venous blood was placed in a plain serum tube and allowed to stand for 30 min at room temperature. Then, the serum was separated by centrifugation at 3000 rpm for 10 min. Analyses of the levels of alanine transaminase (ALT), aspartate transaminase (AST), albumin (ALB), blood urea nitrogen (BUN), creatinine (CREA), creatine kinase (CK), triglyceride (TG), and total bilirubin (TBIL) were performed on the isolated serum using the AU480 Chemistry System (Beckman Coulter, Brea, CA, USA).

2.8. Ethical Approval Statement. Animal experiments were unavoidable to test the biosafety of MM@DOC in order to synthesize more effective drug delivery systems and overcome drug resistance. It is essential for the treatment of NPC patients. All laboratory procedures were approved by the Laboratory Animal Care and Use Committee at the hospital. The animal experiments were performed according to the Animal Ethics Committee of Guangdong Provincial People's Hospital (No. GDREC2019830A). The animals were housed in specific pathogen-free (SPF) and independent air supply cages with a controlled atmosphere, 12-h/12-h dark/light cycle, 18−26 °C, and 45−70% humidity. They were fed

https://doi.org/10.1021/acsomega.4c07132
ACS Omega 2024, 9, 49566−49579

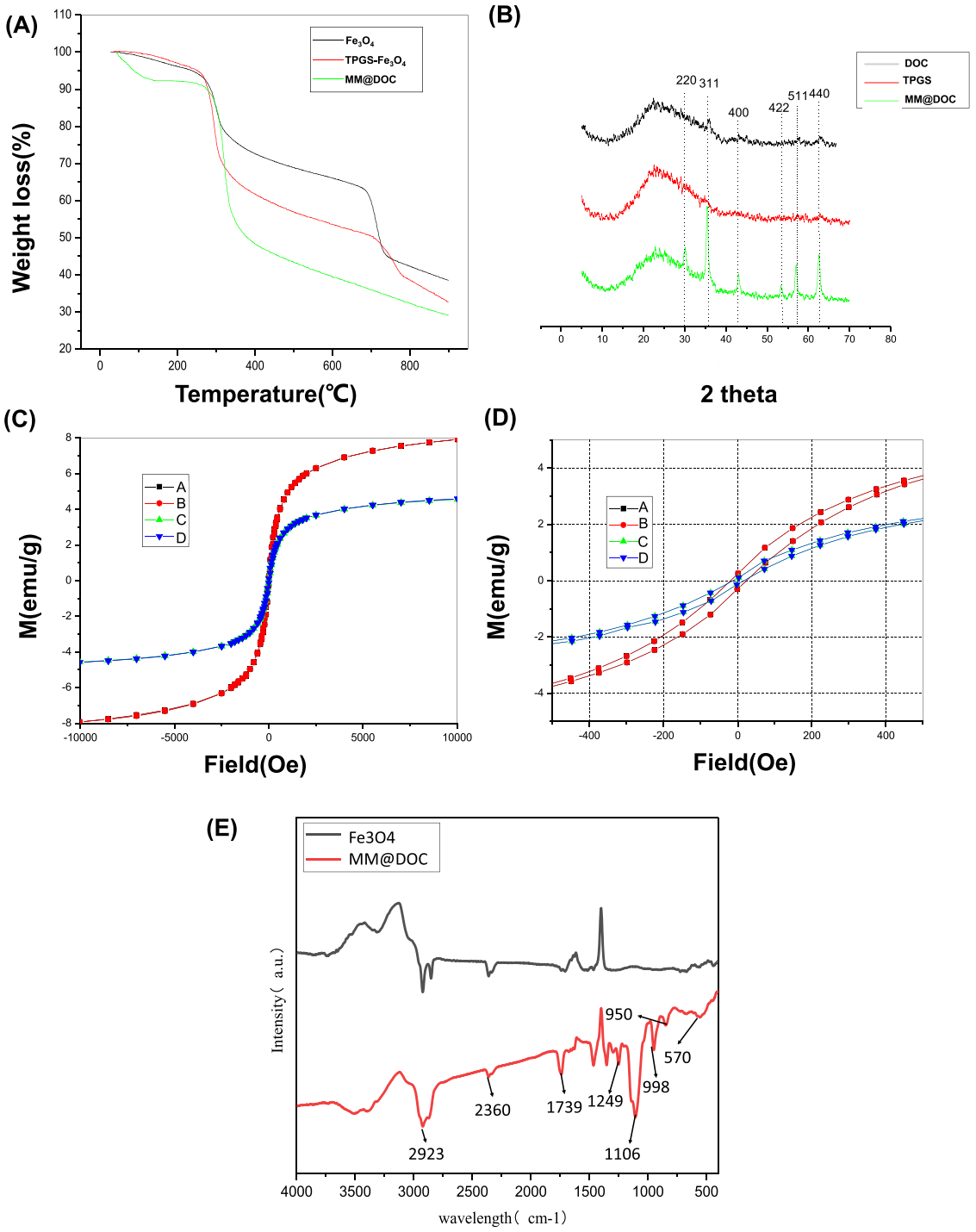

Figure 3. Physical and chemical properties of MM@DOC. (A) Thermal weight loss analysis of MM@DOC. (B) XRD analysis of MM@DOC. (C, D) Magnetization curves of MM@DOC and MNPs (A: MNPs-1, B: MNPs-2; C: MM@DOC-1; D: MM@DOC-2). (E) FTIR spectra of MM@DOC.

standard animal food and water ad libitum. Animal experiments in this study have adhered to the ARRIVE guidelines (https://arriveguidelines.org/). All animals received humane care in compliance with good animal practice according to the animal ethics procedures and guidelines of China.

2.9. Statistical Analysis. Differences between the two groups were determined by a paired-sample *t* test. One-way ANOVA analysis was used to compare the values obtained from multiple groups. GraphPad Prism 8 statistical software was used to process and analyze the experimental data. The differences with $*p < 0.05$, $**p < 0.01$, and $***p < 0.01$ were considered statistically significant.

3. RESULTS

3.1. Characteristics of Multifunctionalized Magnetic Nanocarriers and Composition. The particle size of the MNPs was measured with TEM as shown in Figure 2A. These Fe_3O_4 nanoparticles exhibited a close-packed, almost spherical, black morphology with no discernible precipitates. The MNPs were distributed uniformly and had sizes of 8−10 nm on

https://doi.org/10.1021/acsomega.4c07132
ACS Omega 2024, 9, 49566−49579

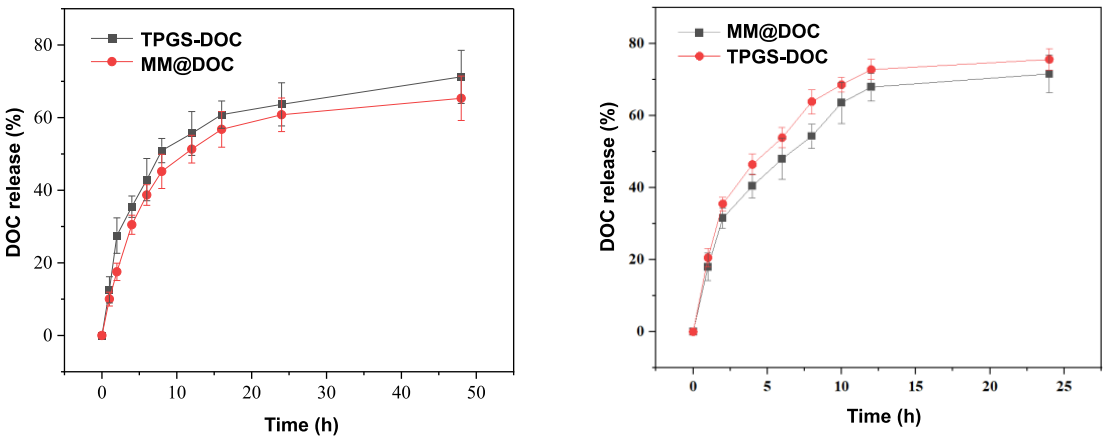

Figure 4. Release kinetics of DOC from TPGS-DOC and MM@DOC at pH 7.4 and 6.8 and at 37 °C.

average. However, MM@DOC had a spherical shape, and the particle size of MM@DOC in TEM Figure 2B was concentrated between 15 and 25 nm, with an aggregation phenomenon. It can be seen that there is a black substance wrapped inside, which is presumed to be MNPs and DOC, which is in line with the morphological structure of the nanoparticles. Figure 2C suggests that the average particle size of MM@DOC was 207.6 nm, and the polydispersity index (PDI) of MM@DOC was 0.180, which can meet the coloading of DOC and MNPs at the nanoscale. However, according to Figure 2D, the average zeta (ζ) potential of the MNPs was +27.27 mV, while for MM@DOC, it was +1.233 mV. There was a significant potential difference between MNPs and MM@DOC, likely resulting from strong magnetic repulsion among the pure MNPs.

TGA was employed to assess the quantity of Fe_3O_4 in the mixed micelles and their heat stability. As shown in Figure 3A, residual water was the cause of the weight loss of Fe_3O_4, TPGS-Fe_3O_4, and MM@DOC during the early stage (0−280 °C). Less than 10% of the initial weight of the three groups had been lost. During this temperature period, the mass ratio of the components did not differ much from that added during the preparation. This indicated that there was not much mass loss during preparation, which proved that the thermal stability of the mixture was satisfactory. The weight loss between 250 and 700 °C was attributed to the thermal degradation of organic components (TPGS and DOC). Consequently, MM@DOC exhibited the most significant weight loss and the steepest curve during this period. The residual weight after 800 °C was counted as inorganic Fe_3O_4 ash.

The structure of MM@DOC was also measured by X-ray powder analysis. The two control groups were pure DOC and pure TPGS. As shown in Figure 3B, six well-resolved reflection peaks of (220), (311), (400), (422), (511), and (440) were observed in mixed micelles, showing a highly ordered structure of Fe_3O_4 nanoparticles in mixed micelles.[32]

Magnetization curves and hysteresis loops of Fe_3O_4 and MM@DOC were measured at 25 °C. As shown in Figure 3C,D, residual magnetic intensity became zero when the external magnetic field was removed. In addition, the shapes of the four hysteresis curves exhibited tight shapes without significant hysteresis losses. No hysteresis curve was observed in the magnetization curves, indicating the superparamagnetic behavior of magnetic micelles, which is similar to Fe_3O_4 nanoparticles. The saturation magnetization value of Fe_3O_4 could reach 7.9 emu/g. After loading in the TPGS micelles, the value of MM@DOC decreased to 4.3 emu/g due to the diamagnetic TPGS layers. For biological purposes, this saturation magnetization level is considered sufficient.

By measuring the absorption of samples at different wavelengths of light, the absorption spectra of MM@DOC and MNPs were obtained, which further analyzed the composition and structure of the substances. Figure 3E depicts the FTIR spectra of MNPs and MM@DOC. The infrared spectrum curve of MM@DOC contained the characteristic curve of MNPs, indicating that MNPs were one of the components of MM@DOC. In addition, MM@DOC exhibited peaks at 1739, 1106, 1249, 998, and 950 cm^{-1}, which were related to the presence of TPGS and DOC.

3.2. Evaluation of Release of MM@DOC In Vitro. The release of DOC from TPGS-DOC and MM@DOC was measured in order to verify efficient release from TPGS micelles in the physiological environment with pH 7.4 and in the tumor environment with pH 6.8 during systemic delivery. The results in Figure 4 show that while there was minimal difference between the two curves representing TPGS-DOC and MM@DOC at pH 7.4 and pH 6.8, TPGS-DOC had a faster release rate than MM@DOC. It may be due to the interaction between Fe_3O_4 and DOC in micelles, thus slowing down the release rate of DOC. However, at pH 7.4, the release rate of the two drugs was fast within 10 h and gradually reached a plateau after 20 h. The release of TPGS-DOC reached 50% at about 8 h, while that of MM@DOC reached 50% at about 10.5 h. Furthermore, the release of TPGS-DOC and MM@DOC reached 72 and 65%, respectively, after 50 h. However, at pH 6.8, a rapid release was also achieved for the first 10 h, and the release leveled off at 12.5 h. MM@DOC reached nearly 50% release after about 7 h. In contrast to the physiological environment, the release rate of MM@DOC is higher in the tumor environment. Therefore, the initial rapid release of MM@DOC ensures the rapid onset of action, while the subsequent slow release prolongs the therapeutic effect of the drug. Also, MM@DOC has a higher release efficiency in the tumor environment.

3.3. In Vitro Cellular Uptake of MM@DOC. Cellular uptake efficiency affects the therapeutic effect of drugs, and we used fluorescence microscopy to observe the uptake intensity of MM@DOC in C666−1/DOC. Figure 5 shows the uptake of MM@DOC by cells in vitro. At the first hour, a trace fluorescence signal was observed. With the increase of time,

https://doi.org/10.1021/acsomega.4c07132
ACS Omega 2024, 9, 49566−49579

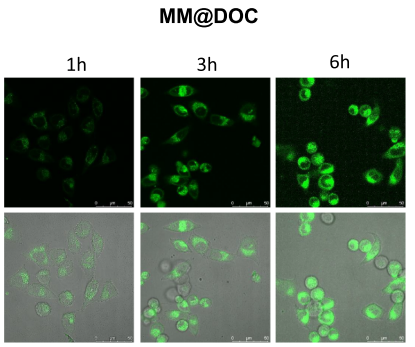

Figure 5. MM@DOC uptake by C666−1/DOC at 1, 3, and 6 h.

the fluorescence signal was gradually enhanced in the cells. The shell of MM@DOC is a TPGS structure. The results confirmed that the TPGS-modified nanodrug delivery system could increase cellular uptake.

3.4. In Vitro Effects of MM@DOC on C666−1/DOC. In order to have a comprehensive evaluation of the biocompatibility of varying concentrations of DOC, TPGS-Fe_3O_4, and MM@DOC, the cytotoxicity of MM@DOC after 24 h of treatment on cancer cells was determined by the MTT assay. In the C666−1/DOC cell line, as shown in Figure 6A, the inhibition rate of cell survival increased with the increase of the concentration of the three substances. As the DOC concentration in MM@DOC increased significantly from 0.1 to 6.4 μg/mL, the cell survival rate decreased from 64.53 ± 2.11 to 56.35 ± 0.62%. The cell survival rate of the MM@DOC group was statistically significantly lower than that of the DOC group at the same concentration of DOC, suggesting that MM@DOC was more hazardous to C666−1/DOC. In addition, when the TPGS concentration reached 115.2 μg/mL, the cell survival rate of the TPGS-Fe_3O_4 group (56.99 ± 2.23%) was slightly different from that of the MM@DOC group (56.35 ± 0.62%). However, the cell viability of the TPGS-Fe_3O_4 and MM@DOC groups was still lower than that of the DOC group. Therefore, more research and discussion are required to understand the mechanism of TPGS-Fe_3O_4's toxicity to C666−1/DOC cells at high concentrations. Overall, at low concentrations (equivalent DOC concentrations of 0.1−0.8 μg/mL and equivalent TPGS concentrations of 1.8−14.4 μg/mL), the cytotoxic effects of MM@DOC were greater than those of pure DOC and TPGS-Fe_3O_4 combined. This suggests that DOC and TPGS-Fe_3O_4 combined to form mixed micelles have better antidrug resistance to tumors.

The percentage of cell apoptosis treated with various formulations of DOC, TPGS-Fe_3O_4, and MM@DOC was determined by a flow cytometer. Based on the results of the MTT experiment, the drug concentration of cell necrosis and apoptosis assay adopted a low concentration. As shown in Figure 6B, the percentage of apoptosis (including early and late apoptosis) of MM@DOC-treated cells was 37.11%. However, compared to the MM@DOC group, the percentage of apoptosis (including early and late apoptosis) in the control, TPGS-Fe_3O_4, and DOC-treated cells was 17.63, 23.09, and 27.30%, respectively. The TPGS-Fe_3O_4 group and the DOC group showed comparable rates of apoptosis; however, the cells treated with MM@DOC were higher in both early and late cell apoptosis. These findings aligned with the cytotoxicity analysis's observed outcomes. Analyzed cytotoxicity data with cell apoptosis data together indicated that DOC modified by

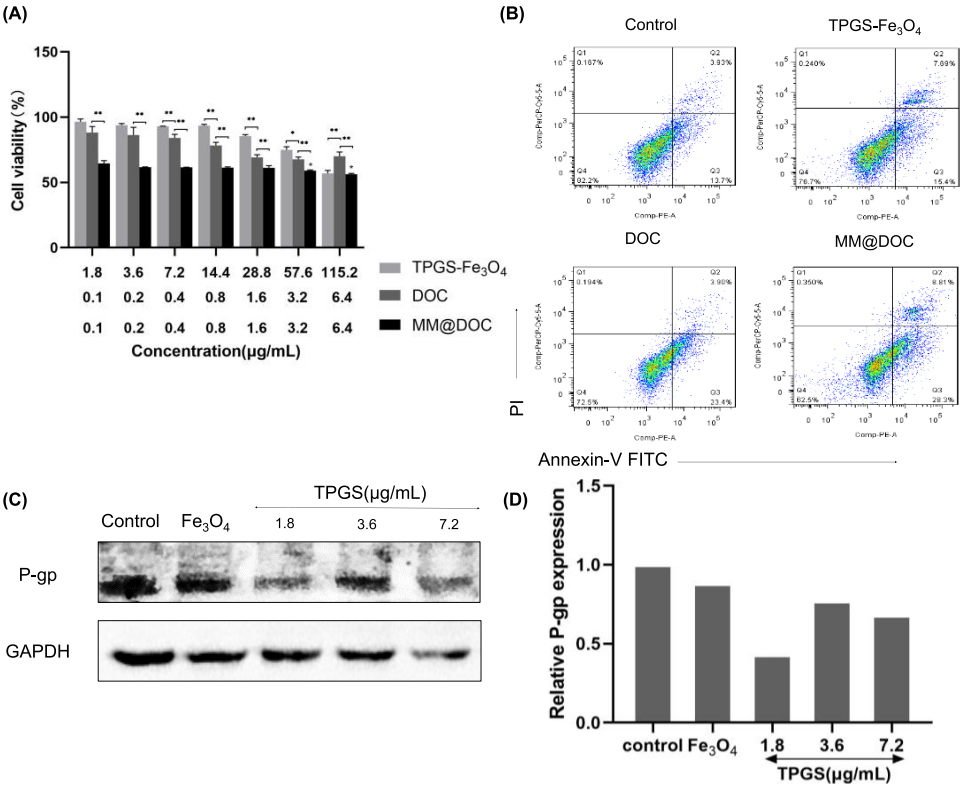

Figure 6. In vitro effects of MM@DOC on C666−1/DOC. (A) MTT results of TPGS-Fe_3O_4, DOC, and MM@DOC at different concentrations on C666−1/DOC cells (n = 3). (B) Apoptosis analysis on C666−1/DOC cells incubated with various samples. (C, D) Western blot for the detection of P-gp expression in response to different formations in C666−1/DOC cells.

https://doi.org/10.1021/acsomega.4c07132
ACS Omega 2024, 9, 49566−49579

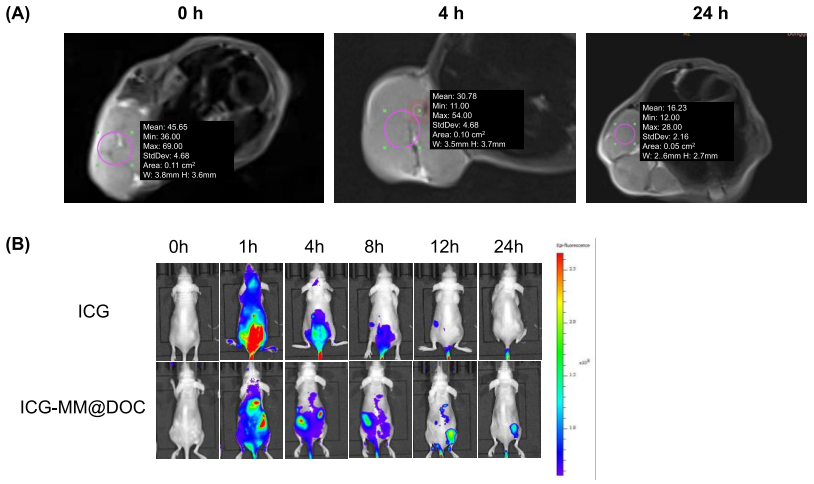

Figure 7. In vivo imaging and drug distribution of MM@DOC. (A) In vivo MRI of C666−1/DOC-bearing nude mice at different times. Purple circles represent the selected tumor regions. **Mean:** average density of tumor images. **Min:** minimum density of tumor images. **Max:** maximum density of tumor images. **StdDev:** standard deviation of tumor image density. **Area:** area of selected tumor regions. **W:** width of selected tumor regions. **H:** height of selected tumor regions. (B) In vivo fluorescence imaging of C666−1/DOC-bearing nude mice at different times.

TPGS has a better cytotoxic effect on DOC-resistant NPC cells and promotes the death of drug-resistant cells. Hence, the application of MM@DOC might be beneficial to overcome the MDR of tumors.

The role of TPGS in reversing drug resistance is attributed to the inhibition of P-gp expression.[36] C666−1/DOC cells were employed in this investigation, with PBS and Fe_3O_4 groups utilized as control groups to rule out the impact of Fe_3O_4 on P-gp expression. Western blot analysis was conducted to assess the impact of TPGS on P-gp protein expression in C666−1/DOC cells. TPGS in the concentration range of 1.8−7.2 μg/mL was used as the experimental group. As shown in Figure 6C, the P-gp bands exhibited a lighter hue at 1.8 and 7.2 μg/mL TPGS concentrations. P-gp was highly expressed in the PBS group and the Fe_3O_4 group (Figure 6D). On the contrary, the expression of P-gp in different concentrations of the TPGS group was downregulated and lower than the PBS group and the Fe_3O_4 group. This indicated that TPGS could inhibit the expression of P-gp protein to increase the concentration of DOC in C666−1/DOC cells and finally reverse the effect of drug resistance. However, there was no correlation between the P-gp protein expression and the TPGS concentration.

3.5. In Vivo Imaging and Drug Distribution. Targeted tissue can rapidly lose its transverse magnetization and look black in T2-weighted mode on magnetic resonance imaging if there is a superparamagnetic material in the tissue.[30] It suggests that distinct density shadows may appear if MM@DOC enters the tumor efficiently. After MM@DOC was injected through the tail vein, an MRI plain scan was performed on the nude mouse tumor model. As Figure 7A shows, the signal of the whole tumor mass visible in the horizontal plane of the tumor body was relatively average. The tumor's mean density at the initial scan (t_0) was 45.65. After 4 h, the mean value decreased from 45.65 ± 4.68 to 30.78 ± 4.68, indicating that MM@DOC could reach the tumor area quickly and darken in MRI. After MM@DOC injection, the mean value decreased to 16.23 ± 2.16 after 24 h. A clear angiographic effect was observed 24 h after injection, and a stronger low-density signal was observed compared to preinjection. These results show that MM@DOC can be used as a contrast agent for NPC and has a good advantage in NPC imaging.

The distribution and metabolic rate of MM@DOC in C666−1/DOC-bearing nude mice were further explored. Fluorescence imaging with ICG as a fluorescent probe was employed to monitor the metabolic distribution of the drug delivery system in vivo (Figure 7B). In the MM@DOC group, strong fluorescence signals were also observed in the liver, heart, and spleen 1 h after administration. In addition, the concentration of MM@DOC in the hepatic and splenic distribution was still higher than that in other parts 4 and 8 h after subsequent administration. However, the fluorescence in the heart decreased significantly after 4 h. Significant fluorescence signals were also observed in the tumor site, which rapidly increased with time, reaching a peak at 12 h postinjection, followed by a slight decrease at 24 h. The concentration of MM@DOC in the tumor did not peak within 8 h of injection, possibly due to tissue blood transport. MM@DOC could reach the tumor within 12 h and undergo gradual metabolism, regardless of the time. In contrast, in the group administered with free ICG, less distribution was observed in the mouse body 8 h after administration, ruling out the effect of the fluorescent agent on MM@DOC. These results indicated that MM@DOC had targeted therapy for tumors. However, it can be seen that MM@DOC could accumulate in high concentrations in vital organs even if the metabolism time was fast. However, the toxic effects of MM@DOC on vital organs need to be ruled out.

3.6. Antitumor Effect of MM@DOC In Vivo. The underlying mechanisms of NPC resistance are lacking. The hypothesis of this study is that P-gp protein overexpression contributes to NPC drug resistance. Based on the in vitro experiment, MM@DOC showed excellent cytotoxicity to C666−1/DOC cells. In the WB experiment, MM@DOC could inhibit the expression of P-gp protein. MM@DOC was injected into tumor-bearing mice via the tail vein in order to investigate the tumor therapeutic impact of MM@DOC in vivo. The body weight and tumor volume of the mice were measured every other day. After the final dosage, the tumors were aseptically excised and photographed in order to be weighed, as shown in Figure 8. After 30 days of drug

https://doi.org/10.1021/acsomega.4c07132
ACS Omega 2024, 9, 49566−49579

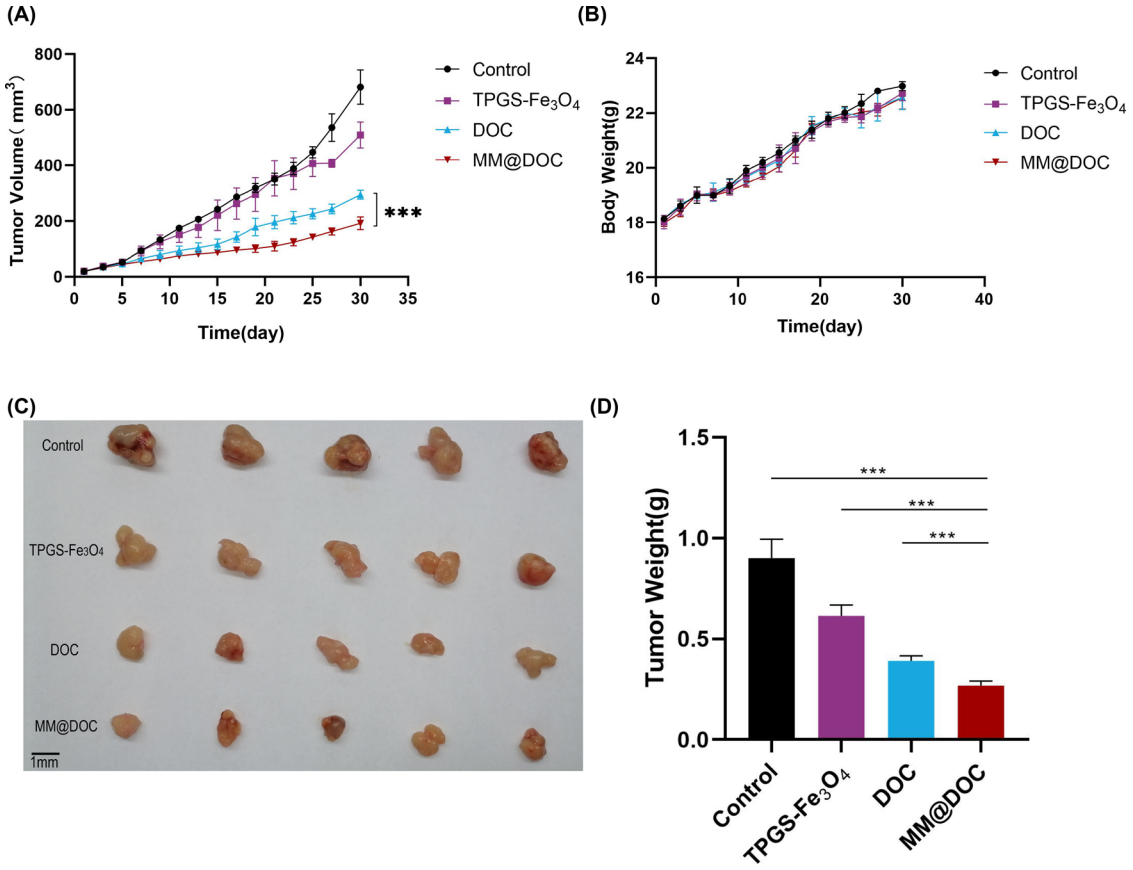

Figure 8. In vivo antitumor effect of MM@DOC. (A) Tumor volume changes after treatment with PBS, TPGS-Fe_3O_4, DOC, and MM@DOC in 30 days. (B) Tumor-bearing mice's body weight after treatment with PBS, TPGS-Fe_3O_4, DOC, and MM@DOC in 30 days. (C) Representative tumor images on day 30. (D) Tumor weight of different treatment groups on day 30.

administration, to observe the changes in tumor volume among the groups, the recorded tumor volume was made into a line chart with time as the abscissa and tumor volume as the ordinate (Figure 8A). The average tumor volume of the TPGS-Fe_3O_4 group, DOC group, and MM@DOC group grew from 19.42 ± 1.59 mm^3, 19.20 ± 2.32 mm^3, and 19.541 ± 1.67 mm^3 to 507.79 ± 46.54 mm^3, 294.17 ± 16.05 mm^3, and 191.70 ± 22.89 mm^3, respectively. As a control group, the average tumor volume of the PBS group increased from 19.25 ± 0.42 to 681.43 ± 61.47 mm^3. The curves of the blank group and the TPGS-Fe_3O_4 group were consistent in the line chart before 25 days, indicating that TPGS-Fe_3O_4 had no obvious antitumor effect in vivo. The tumor volumes of the DOC group and MM@DOC group grew relatively slowly after administration, and both groups were statistically significant compared with the control group and TPGS-Fe_3O_4 group. According to the tumor volume statistics, MM@DOC showed a more obvious antitumor effect, and there was statistical significance compared with DOC. After 30 days, the excised tumors were photographed and weighed (Figure 8C,D). The weight of the MM@DOC group (0.268 ± 0.094 g) was significantly reduced, which was statistically significant compared to that of the DOC group (0.390 ± 0.025 g). It can be concluded that MM@DOC had a similar antitumor effect in reducing tumor body weight. During the administration period, the weight gain changes of the four groups of mice were similar (Figure 8B), indicating that each drug had no significant effect on the growth of the mice. Furthermore, no mice died during the experiment.

3.7. Biosafety Evaluation of MM@DOC. Mice venous blood was drawn to measure eight liver and kidney function indicators, including ALB, ALT, AST, BUN, CK, CREA, TBIL, and TG, in order to confirm the biological safety of MM@DOC. ALB, AST, ALT, and TBIL can reflect the condition of liver function. CREA, BUN, and TG can show the condition of renal function. CK can reflect cardiac function. Figure 9 shows that the MM@DOC group had higher ALB, AST, and TBIL indexes than the control group, but only the rise in AST was statistically significant. It can be inferred that the liver of the mice treated with MM@DOC was not too much impaired. CREA in the MM@DOC group was slightly higher than that in the control group, but there was no statistical significance, while BUN and TG values were lower than those in the control group, which might indicate that MM@DOC did not show renal toxicity. The statistically significant increase of the CK value indicated that MM@DOC may have some cardiac function damage, which is consistent with the results of in vivo imaging in nude mice, which showed that MM@DOC could be distributed in the liver and heart. In conclusion, MM@DOC had certain toxicity to important organs such as the heart and liver, but it is only reflected in CK and AST values.

4. DISCUSSION

At present, DOC is a first-line drug for treating advanced malignant tumors. DOC exerts its antitumor effect by entering tumor cells and inhibiting cell cycle progression.[10] However, being hydrophobic, DOC exhibits significant adverse reactions in the biological environment, ultimately resulting in low drug

https://doi.org/10.1021/acsomega.4c07132
ACS Omega 2024, 9, 49566−49579

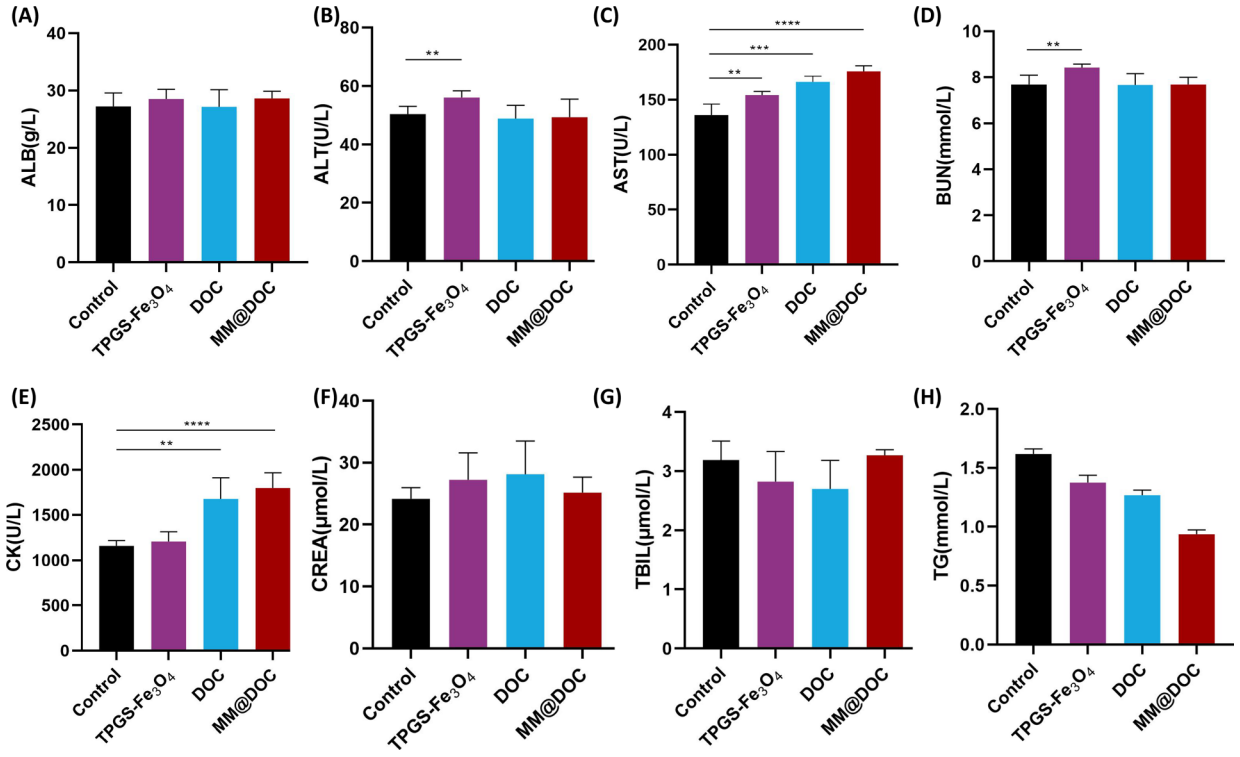

Figure 9. Biochemical analysis including (A) albumin (ALB), (B) alanine transaminase (ALT), (C) aspartate transaminase (AST), (D) blood urea nitrogen (BUN), (E) creatine kinase (CK), (F) creatinine (CREA), (G) total bilirubin (TBIL), and (H) triglyceride (TG) blood route analysis of the mice after treatment with PBS, TPGS-Fe_3O_4, DOC, and MM@DOC on day 30.

utilization.[37,38] Long-term use of DOC leads to the emergence of MDR in malignant tumors, which has become a common problem in cervical cancer, breast cancer, prostate cancer, and colorectal cancer. DOC is also a preferred drug for treating head and neck tumors. Single-agent therapy greatly reduces the therapeutic effect of drug-resistant tumors. Since drugs are released in a stimulatory response, prodrug nanoparticles have been explored as an effective means of drug delivery. Previous studies have demonstrated drug delivery to target organelles by direct release of drugs into mitochondria in response to pH and light.[39] However, there is still insufficient exploration of the resistance mechanism in NPC. In this study, TPGS micelles were loaded with MNPs and DOC to target and diagnose MDR tumors (MM@DOC). We selected C666−1 NPC cells and developed DOC-resistant variants by exposing them to low doses of the drug over an extended period. In vitro experiments suggest that MM@DOC exhibits strong cytotoxicity against C666−1/DOC cells. Furthermore, Western blot experiments in this study demonstrate that TPGS down-regulates P-gp expression, reducing DOC efflux and thereby reversing the resistance of C666−1/DOC cells. Additionally, in vivo, the results indicated that MM@DOC was more effective in inhibiting tumor growth compared to treatment with DOC or TPGS alone. The results of biochemical assays demonstrated that MM@DOC exhibited minimal damage to vital organs.

The processes involved in drug resistance can be broadly classified into five categories: growth factors, genetic factors, xenobiotic metabolism, DNA repair capability, and drug efflux.[15] In cancer therapy, TPGS inhibits P-gp by reducing its ATPase activity, which leads to the reduction of drug efflux from cells.[9] Western blot analysis in this experiment indicates that the expression of P-gp decreased after treatment with TPGS in C666−1/DOC cells compared to that of the control and Fe_3O_4 groups. However, there was no concentration-dependent trend in P-gp expression observed after treatment with three different concentrations of TPGS (1.8, 3.6, and 7.2 μg/mL). This observation may be attributed to the selected concentration range of TPGS. In the MTT experiment, no statistically significant difference in cytotoxicity was observed between the low concentrations of MM@DOC groups. While a statistically significant difference in cytotoxicity was observed when the TPGS concentration in MM@DOC reached 57.6 μg/mL. Liang and colleagues[40] also built TPGS-based drug delivery systems to reverse breast cancer resistance. Their experiment confirmed the down-regulation of intracellular P-gp which can mediate drug efflux leading to drug resistance after the addition of TPGS. Du and colleagues discovered that both TPGS and nitric oxide (NO) could inhibit P-gp protein expression in doxorubicin (DOX)-resistant liver cancer cells, thereby reversing drug resistance.[41] In addition, Li and colleagues[42] obtained the same outcomes in trials of reverse cervical cancer resistance. Therefore, it is not an accident that TPGS reverses drug resistance. This study confirmed a decrease in the level of P-gp expression after TPGS addition, consistent with prior experimental findings. TPGS has good biocompatibility, but the DOC enrichment of TPGS arriving at the tumor site as a shell should be considered. Some studies have used the characteristics of tumor environment immunity to construct natural pH-unstable artificial NK cells using mesoporous silicon nanoparticles as scaffolds, wherein DOX was effectively enriched in the tumor site.[43] Although MM@DOC had a higher release efficiency in the tumor environment (pH 6.8), tumor immune characteristics were not taken into account. Drug resistance to DOC has been observed, and numerous reports have verified that the overexpression of P-gp

https://doi.org/10.1021/acsomega.4c07132
ACS Omega 2024, 9, 49566−49579

is strongly linked to the mechanism of drug resistance.[16−18] However, it is important to note that not all instances of tumor resistance are attributed to changes in P-gp expression. Although DOC is a significant chemotherapeutic medication for NPC, there has been limited investigation into the mechanisms underlying drug resistance that arises in NPC. Consequently, even if DOC resistance is present in NPC, its molecular mechanism is still unknown. In the study of paclitaxel-resistant human ovarian cancer cells, Kumar and colleagues[44] found no expression of the MDR1 gene, which encodes the expression of P-g. However, in subsequent studies, Wu and colleagues[45] found that P-gp was expressed in human NPC cells. In addition, Zhou and colleagues[34] and Hou and colleagues[33] proved that ABC transporters contribute to paclitaxel resistance in NPC cells. For DOC to exert its antitumor effect, it must enter the cells. The level of drug uptake is correlated to the expression level of P-gp. The underlying hypothesis of this study was that there exists an association between P-gp expression and DOC resistance in NPC. In this study, TPGS decreased the expression of P-gp in C666−1/DOC cells in the Western blot assay. In addition, MM@DOC has shown the ability to reverse drug resistance in apoptosis, cytotoxicity, and in vivo antitumor tests. These findings might support the validity of the idea.

TPGS is a promising catalyst for reverse drug resistance. However, it has to be investigated whether TPGS could potentially make chemotherapy medications more harmful to normal cells during treatment. In this study, the proportion of TPGS in the mixture was 18 times that of chemotherapy drugs. In the cytotoxicity test, TPGS-Fe_3O_4 showed minimal difference from MM@DOC when the TPGS concentration was 115.2 μg/mL. Further experiments are required to investigate whether high concentrations of TPGS, Fe_3O_4, or their combination cause cytotoxicity, which has not been shown at lower concentrations of TPGS-Fe_3O_4. Furthermore, in vivo fluorescence imaging demonstrated that although MM@DOC in the heart was rapidly degraded, it remained accumulated in the liver and spleen for an extended period of time. The spleen and liver have greater TPGS concentrations due to high blood perfusion rates and high reticuloendothelial system (RES) expression, while the heart and kidney have substantially lower levels of TPGS, which is probably due to low expression of the RES in these organs.[36] Additionally, in vivo data demonstrated that TPGS by itself had little inhibitory effect on tumor masses. From the perspective of venous blood indexes, although the liver damage index was higher when TPGS was used alone, there was no obvious hepatorenal toxicity of MM@DOC. In the TPGS combined with DOX to inhibit drug-resistant liver cancer system, H&E staining revealed that apart from damaging tumor tissues, there was no harm to other organs.[41] Likewise, in TPGS-reversal-resistant breast cancer research, it was indicated that TPGS posed no toxicity to vital organs such as the mouse heart, kidney, and liver.[46] Meanwhile, there was no death or weight loss during the treatment, and the mice maintained good physical and mental condition. In conclusion, whether TPGS alone or TPGS combined with DOC, there is no strong toxicity to vital organs, and its safety can be recognized. In addition, photothermal therapy combined with chemotherapy can effectively inhibit tumor proliferation, and iron provides a photothermal effect. A platelet-based biohybrid delivery system that integrates photothermal, reactive oxygen species (ROS)-responsive therapeutic nanoparticles and MNPs into platelets has been synthesized to enable drugs to cross the blood−brain barrier to inhibit glioma growth. MNPs were also encapsulated in MM@DOC, but the role of MM@DOC in photothermotherapy of drug-resistant NPC was lacking in this study.[47]

MDR is becoming an increasingly common clinical challenge, affecting the administration of chemotherapeutic medications. Therefore, the goal of this research is to find a solution to drug resistance. We built a new drug delivery system for reversing drug resistance, which is also helpful for imaging diagnosis of tumors and also provides some new ideas for exploring the mechanism of drug resistance in NPC.

5. CONCLUSIONS

In this study, a novel complex (MM@DOC) was synthesized from TPGS micelles loaded with DOC and MNPs in order to reduce tumor drug resistance and improve tumor imaging. This drug delivery system reverses drug resistance by inhibiting the expression of P-gp to reduce drug efflux. Both in vitro and in vivo experiments showed that MM@DOC exhibited enhanced cytotoxicity and potent antitumor efficacy. According to these results, TPGS could potentially serve as a valuable platform for the delivery and encapsulation of some chemotherapeutic medications. This is especially true when it comes to drug-resistant malignancies since TPGS may help reverse drug resistance by blocking P-gp activity. In conclusion, MM@DOC synthesized in this study is not only superior in the treatment of drug-resistant tumors but also superior in the diagnosis of tumors, which can be regarded as a safe and effective multifunctional drug delivery system.

■ ASSOCIATED CONTENT

Supporting Information

The Supporting Information is available free of charge at https://pubs.acs.org/doi/10.1021/acsomega.4c07132.

Detailed experimental procedures and cell survival rate data of C666−1/DOC cells (PDF)

■ AUTHOR INFORMATION

Corresponding Authors

Jun-Zheng Li − *Department of Otolaryngology-Head and Neck Surgery, Zhujiang Hospital of Southern Medical University, Guangzhou 510280, China*; Phone: +86-18928900393; Email: jzli2002@163.com; Fax: +86-18928900393

Guan-Hai Wang − *School of Pharmacy, Guangdong Medical University, Dongguan 523808, China*; orcid.org/0000-0002-7087-4622; Phone: +86-15118359628; Email: wangguanhai@gdmu.edu.cn; Fax: +86-15118359628

Tao Liu − *Department of Otolaryngology-Head and Neck Surgery, Guangdong Provincial People's Hospital (Guangdong Academy of Medical Sciences), Southern Medical University, Guangzhou 510080, China*; orcid.org/0000-0001-8735-0115; Phone: +86-15627864803; Email: taoliu18@126.com; Fax: +86-15627864803

Authors

Hui-Qin Liu − *Department of Otolaryngology-Head and Neck Surgery, Guangdong Provincial People's Hospital (Guangdong Academy of Medical Sciences), Southern*

https://doi.org/10.1021/acsomega.4c07132
ACS Omega 2024, 9, 49566−49579

Medical University, Guangzhou 510080, China; Shantou University Medical College, Shantou, Guangdong 515063, China; orcid.org/0009-0003-6790-2439

Xi-Dong Wu − *Department of Drug Safety Evaluation, Jiangxi Testing Center of Medical Instruments, Nanchang 330029, China*

Xue-Wen Fang − *Department of Radiology, The Tenth Affiliated Hospital of Southern Medical University (Dongguan People's Hospital), Dongguan 523059, China*

Yun-Song An − *Department of Otolaryngology-Head and Neck Surgery, Guangdong Provincial People's Hospital (Guangdong Academy of Medical Sciences), Southern Medical University, Guangzhou 510080, China*

Meng Xia − *Department of Otolaryngology-Head and Neck Surgery, Zhujiang Hospital of Southern Medical University, Guangzhou 510280, China*

Xiao-Hua Luo − *Department of Otolaryngology-Head and Neck Surgery, Zhujiang Hospital of Southern Medical University, Guangzhou 510280, China*

Complete contact information is available at: https://pubs.acs.org/10.1021/acsomega.4c07132

Author Contributions

[▽]H.-Q.L., X.-D.W., and X.-W.F. are the cofirst authors and have contributed equally to this work.

Notes

The authors declare no competing financial interest.

■ ACKNOWLEDGMENTS

This work was financially supported by the Science and Technology Program of Guangzhou City [202002030065 and 202102010041], the Natural Science Foundation of Guangdong Province [2019A1515011678], the matching scientific research fund for Guangdong Provincial Outstanding Young Medical Talent by Guangdong Provincial People's Hospital [KJ012019454], Dongguan Science and Technology of Social Development Program [20211800905062], Zhanjiang Competitive Special Fund for Science and Technology Development [2021A05047], Guangdong Basic and Applied Basic Research Foundation [2021A1515111168], and Science and Technology Plan Project of Guangzhou [202102020846].

■ REFERENCES

(1) Chen, Y. P.; Chan, A. T. C.; Le, Q. T.; Blanchard, P.; Sun, Y.; Ma, J. Nasopharyngeal carcinoma. *Lancet* **2019**, *394* (10192), 64−80.

(2) Lam, W. K. J.; Chan, J. Y. K. Recent advances in the management of nasopharyngeal carcinoma. *F1000Research* **2018**, *7*, F1000.

(3) Guan, S.; Wei, J.; Huang, L.; Wu, L. Chemotherapy and chemoresistance in nasopharyngeal carcinoma. *European journal of medicinal chemistry* **2020**, *207*, No. 112758.

(4) Wang, R.; Wu, F.; Lu, H.; Wei, B.; Feng, G.; Li, G.; Liu, M.; Yan, H.; Zhu, J.; Zhang, Y.; et al. Definitive intensity-modulated radiation therapy for nasopharyngeal carcinoma: long-term outcome of a multicenter prospective study. *J. Cancer Res. Clin Oncol* **2013**, *139* (1), 139−145.

(5) Wang, W.; Zhou, S.; Cheng, Z.; Ma, D.; Liu, T. A glutathione-sensitive cationic polymer delivery of CRISPR-Cas9 RNA plasmid for targeting nasopharyngeal carcinoma gene therapy. *Colloids Surf. B Biointerfaces* **2023**, *223*, No. 113146.

(6) Leong, S. S.; Wee, J.; Rajan, S.; Toh, C. K.; Lim, W. T.; Hee, S. W.; Tay, M. H.; Poon, D.; Tan, E. H. Triplet combination of gemcitabine, paclitaxel, and carboplatin followed by maintenance 5-fluorouracil and folinic acid in patients with metastatic nasopharyngeal carcinoma. *Cancer* **2008**, *113* (6), 1332−1337.

(7) Tan, E. H.; Khoo, K. S.; Wee, J.; Fong, K. W.; Lee, K. S.; Lee, K. M.; Chua, E. T.; Tan, T.; Khoo-Tan, H. S.; Yang, T. L.; et al. Phase II trial of a paclitaxel and carboplatin combination in Asian patients with metastatic nasopharyngeal carcinoma. *Ann. Oncol* **1999**, *10* (2), 235−237.

(8) Leong, S. S.; Wee, J.; Tay, M. H.; Toh, C. K.; Tan, S. B.; Thng, C. H.; Foo, K. F.; Lim, W. T.; Tan, T.; Tan, E. H. Paclitaxel, carboplatin, and gemcitabine in metastatic nasopharyngeal carcinoma: a Phase II trial using a triplet combination. *Cancer* **2005**, *103* (3), 569−575.

(9) Gorain, B.; Choudhury, H.; Pandey, M.; Kesharwani, P. Paclitaxel loaded vitamin E-TPGS nanoparticles for cancer therapy. *Materials Science and Engineering: C* **2018**, *91*, 868−880.

(10) Cortes, J. E.; Pazdur, R. Docetaxel. *J. Clin Oncol* **1995**, *13* (10), 2643−2655.

(11) Rowinsky, E. K. The development and clinical utility of the taxane class of antimicrotubule chemotherapy agents. *Annu. Rev. Med.* **1997**, *48*, 353−374.

(12) Kaushik, L.; Srivastava, S.; Panjeta, A.; Chaudhari, D.; Ghadi, R.; Kuche, K.; Malik, R.; Preet, S.; Jain, S.; Raza, K. Exploration of docetaxel palmitate and its solid lipid nanoparticles as a novel option for alleviating the rising concern of multi-drug resistance. *Int. J. Pharm.* **2020**, *578*, No. 119088.

(13) Xu, W.; Wang, J.; Li, Q.; Wu, C.; Wu, L.; Li, K.; Li, Q.; Han, Q.; Zhu, J.; Bai, Y.; et al. Cancer cell membrane-coated nanogels as a redox/pH dual-responsive drug carrier for tumor-targeted therapy. *J. Mater. Chem. B* **2021**, *9* (38), 8031−8037.

(14) Assaraf, Y. G.; Brozovic, A.; Gonçalves, A. C.; Jurkovicova, D.; Linē, A.; Machuqueiro, M.; Saponara, S.; Sarmento-Ribeiro, A. B.; Xavier, C. P. R.; Vasconcelos, M. H. The multi-factorial nature of clinical multidrug resistance in cancer. *Drug Resist. Updates* **2019**, *46*, No. 100645.

(15) Bukowski, K.; Kciuk, M.; Kontek, R. Mechanisms of Multidrug Resistance in Cancer Chemotherapy. *Int. J. Mol. Sci.* **2020**, *21* (9), 3233.

(16) Eckford, P. D.; Sharom, F. J. ABC efflux pump-based resistance to chemotherapy drugs. *Chem. Rev.* **2009**, *109* (7), 2989−3011.

(17) Sun, Y. L.; Patel, A.; Kumar, P.; Chen, Z. S. Role of ABC transporters in cancer chemotherapy. *Chin. J. Cancer* **2012**, *21* (2), 51−57.

(18) Smith, E. R.; Wang, J. Q.; Yang, D. H.; Xu, X. X. Paclitaxel resistance related to nuclear envelope structural sturdiness. *Drug Resist Updat* **2022**, *65*, No. 100881.

(19) Lin, J.-T.; Zou, Y.; Wang, C.; Zhong, Y.-C.; Zhao, Y.; Zhu, H.-E.; Wang, G.-H.; Zhang, L.-M.; Zheng, X.-B. Cationic micellar nanoparticles for DNA and doxorubicin co-delivery. *Materials Science and Engineering: C* **2014**, *44*, 430−439.

(20) Robey, R. W.; Pluchino, K. M.; Hall, M. D.; Fojo, A. T.; Bates, S. E.; Gottesman, M. M. Revisiting the role of ABC transporters in multidrug-resistant cancer. *Nat. Rev. Cancer* **2018**, *18* (7), 452−464.

(21) Wang, X.; Zhang, H.; Chen, X. Drug resistance and combating drug resistance in cancer. *Cancer Drug Resist.* **2019**, *2* (2), 141−160.

(22) Zhu, Y. X.; Jia, H. R.; Duan, Q. Y.; Wu, F. G. Nanomedicines for combating multidrug resistance of cancer. *Wiley Interdiscip. Rev.: Nanomed. Nanobiotechnol.* **2021**, *13* (5), No. e1715.

(23) Wang, W.; Zhou, M.; Xu, Y.; Peng, W.; Zhang, S.; Li, R.; Zhang, H.; Zhang, H.; Cheng, S.; Wang, Y.; et al. Resveratrol-Loaded TPGS-Resveratrol-Solid Lipid Nanoparticles for Multidrug-Resistant Therapy of Breast Cancer: In Vivo and In Vitro Study. *Front. Bioeng. Biotechnol.* **2021**, *9*, No. 762489.

(24) Du, B.; Zhu, W.; Yu, L.; Wang, Y.; Zheng, M.; Huang, J.; Shen, G.; Zhou, J.; Yao, H. TPGS2k-PLGA composite nanoparticles by depleting lipid rafts in colon cancer cells for overcoming drug resistance. *Nanomed.: Nanotechnol., Biol. Med.* **2021**, *35*, No. 102307.

(25) Rathod, S.; Bahadur, P.; Tiwari, S. Nanocarriers based on vitamin E-TPGS: design principle and molecular insights into

improving the efficacy of anticancer drugs. *Int. J. Pharm.* **2021**, *592*, No. 120045.
(26) Tu, Y.; Zhang, W.; Fan, G.; Zou, C.; Zhang, J.; Wu, N.; Ding, J.; Zou, W. Q.; Xiao, H.; Tan, S. Paclitaxel-loaded ROS-responsive nanoparticles for head and neck cancer therapy. *Drug Delivery* **2023**, *30* (1), No. 2189106.
(27) Zhang, Z.; Tan, S.; Feng, S. S. Vitamin E TPGS as a molecular biomaterial for drug delivery. *Biomaterials* **2012**, *33* (19), 4889−4906.
(28) Hu, X.; Li, R.; Wu, W.; Fang, K.; Zhu, Z.; Wang, Y.; Zhou, L.; Chen, M.; Dong, C.; Shi, S. A Fe(III)-porphyrin-oxaliplatin(IV) nanoplatform for enhanced ferroptosis and combined therapy. *J. Controlled Release* **2022**, *348*, 660−671.
(29) Hu, Y.; Mignani, S.; Majoral, J. P.; Shen, M.; Shi, X. Construction of iron oxide nanoparticle-based hybrid platforms for tumor imaging and therapy. *Chem. Soc. Rev.* **2018**, *47* (5), 1874−1900.
(30) Farzin, A.; Etesami, S. A.; Quint, J.; Memic, A.; Tamayol, A. Magnetic Nanoparticles in Cancer Therapy and Diagnosis. *Adv. Healthcare Mater.* **2020**, *9* (9), No. e1901058.
(31) Gobbo, O. L.; Sjaastad, K.; Radomski, M. W.; Volkov, Y.; Prina-Mello, A. Magnetic Nanoparticles in Cancer Theranostics. *Theranostics* **2015**, *5* (11), 1249−1263.
(32) Lu, A. H.; Salabas, E. L.; Schüth, F. Magnetic nanoparticles: synthesis, protection, functionalization, and application. *Angew. Chem., Int. Ed. Engl.* **2007**, *46* (8), 1222−1244.
(33) Hou, Y.; Zhu, Q.; Li, Z.; Peng, Y.; Yu, X.; Yuan, B.; Liu, Y.; Liu, Y.; Yin, L.; Peng, Y.; et al. The FOXM1-ABCC5 axis contributes to paclitaxel resistance in nasopharyngeal carcinoma cells. *Cell Death Dis* **2017**, *8* (3), No. e2659.
(34) Zhou, Z.; Zhang, L.; Xie, B.; Wang, X.; Yang, X.; Ding, N.; Zhang, J.; Liu, Q.; Tan, G.; Feng, D.; et al. FOXC2 promotes chemoresistance in nasopharyngeal carcinomas via induction of epithelial mesenchymal transition. *Cancer Lett.* **2015**, *363* (2), 137−145.
(35) Wang, H.; Li, X.; Tse, B. W.; Yang, H.; Thorling, C. A.; Liu, Y.; Touraud, M.; Chouane, J. B.; Liu, X.; Roberts, M. S.; et al. Indocyanine green-incorporating nanoparticles for cancer theranostics. *Theranostics* **2018**, *8* (5), 1227−1242.
(36) Mehata, A. K.; Setia, A.; Vikas; Malik, A. K.; Hassani, R.; Dailah, H. G.; Alhazmi, H. A.; Albarraq, A. A.; Mohan, S.; Muthu, M. S. Vitamin E TPGS-Based Nanomedicine, Nanotheranostics, and Targeted Drug Delivery: Past, Present, and Future. *Pharmaceutics* **2023**, *15* (3), 722.
(37) Alfaleh, M. A.; Hashem, A. M.; Abujamel, T. S.; Alhakamy, N. A.; Kalam, M. A.; Riadi, Y.; Shadab, M. Apigenin Loaded Lipoid−PLGA−TPGS Nanoparticles for Colon Cancer Therapy: Characterization, Sustained Release, Cytotoxicity, and Apoptosis Pathways. *Polymers* **2022**, *14* (17), 3577.
(38) Tang, L.; Huang, K.; Jiang, W.; Fu, L.; Zhang, R.; Shen, L.; Ou, Z.; Huang, Y.; Zhang, Z. Exploration of the inhibition action of TPGS on tumor cells and its combined use with chemotherapy drugs. *Drug Delivery* **2023**, *30* (1), No. 2183830.
(39) Xu, R.; Zhu, E.; Lan, X.; Yang, Q.; Zhang, C. Mitochondrial targeted prodrug nanoparticles for chemo-photodynamic combinational tumour therapy. *Smart Materials in Medicine* **2024**, *5* (3), 373−385.
(40) Liang, L.; Peng, Y.; Qiu, L. Mitochondria-targeted vitamin E succinate delivery for reversal of multidrug resistance. *J. Controlled Release* **2021**, *337*, 117−131.
(41) Du, Z.; Mao, Y.; Zhang, P.; Hu, J.; Fu, J.; You, Q.; Yin, J. TPGS-Galactose-Modified Polydopamine Co-delivery Nanoparticles of Nitric Oxide Donor and Doxorubicin for Targeted Chemo-Photothermal Therapy against Drug-Resistant Hepatocellular Carcinoma. *ACS Appl. Mater. Interfaces* **2021**, *13* (30), 35518−35532.
(42) Li, L.; Liu, T.; Liao, J. X.; Zhang, Z. Y.; Song, D. B.; Wang, G. H. Dual-responsive TPGS crosslinked nanocarriers to overcome multidrug resistance. *J. Mater. Chem. B* **2020**, *8* (36), 8383−8394.
(43) Li, Q.; Shi, Z.; Ou, M.; Li, Z.; Luo, M.; Wu, M.; Dong, X.; Lu, L.; Lv, F.; Zhang, F.; et al. pH-labile artificial natural killer cells for overcoming tumor drug resistance. *J. Controlled Release* **2022**, *352*, 450−458.
(44) Kumar, A.; Soprano, D. R.; Parekh, H. K. Cross-resistance to the synthetic retinoid CD437 in a paclitaxel-resistant human ovarian carcinoma cell line is independent of the overexpression of retinoic acid receptor-gamma. *Cancer Res.* **2001**, *61* (20), 7552−7555.
(45) Wu, R. W. K.; Chu, E. S. M.; Huang, Z.; Xu, C. S.; Ip, C. W.; Yow, C. M. N. Effect of FosPeg mediated photoactivation on P-gp/ABCB1 protein expression in human nasopharyngeal carcinoma cells. *J. Photochem. Photobiol., B* **2015**, *2015* (148), 82−87.
(46) Liu, S.; Li, R.; Qian, J.; Sun, J.; Li, G.; Shen, J.; Xie, Y. Combination Therapy of Doxorubicin and Quercetin on Multidrug-Resistant Breast Cancer and Their Sequential Delivery by Reduction-Sensitive Hyaluronic Acid-Based Conjugate/d-alpha-Tocopheryl Poly(ethylene glycol) 1000 Succinate Mixed Micelles. *Mol. Pharmaceutics* **2020**, *17* (4), 1415−1427.
(47) Jiang, Z.; Zhang, H.; Zhang, W.; Zhang, Y.; Cui, Y.; Mei, L.; Wang, Q. Smart platelet-based biohybrid delivery system for magnetic-guided targeted delivery and enhanced photothermal-chemo therapy against glioma. *Nano Today* **2024**, *56*, No. 102295.

https://doi.org/10.1021/acsomega.4c07132
ACS Omega 2024, 9, 49566−49579